

ORIGINAL RESEARCH ARTICLE

Machine learning-enabled prediction and inverse screening of elastic modulus in Euclidean-tiling structures

Zongze Wu^{1,2} , Xiaoxiao Dong^{2,3} , Lei Cao^{2,4} , Deliang Zhang^{1*} ,
and Xing Zhang^{2,4*} 

¹School of Materials Science and Engineering, Northeastern University, Shenyang, Liaoning, China

²Shenyang National Laboratory for Materials Science, Institute of Metal Research, Chinese Academy of Sciences, Shenyang, Liaoning, China

³College of Mechanical Engineering, Liaoning Petrochemical University, Fushun, Liaoning, China

⁴School of Materials Science and Engineering, University of Science and Technology of China, Shenyang, Liaoning, China

Abstract

Traditional bone-implant lattices are commonly based on periodic unit cells, which simplify design and fabrication but limit geometric diversity and the fine, directional tuning of effective stiffness. Herein, a data-driven framework for multi-cell tessellations inspired by Euclidean-tiling (ET) is proposed to balance geometric freedom with controllable in-plane elastic modulus. Using three tiling-compatible unit cells (tris, quad, and oct), 10,000 randomly assembled 5×5 tiling structures were generated to construct a finite element database of structure-property relationships targeting the in-plane equivalent modulus (E_x and E_y). A fully connected neural network (FCNN) was trained with two input feature representations, namely a unit cell arrangement encoding (UCAE) and a unit cell frequency statistic (UCFS). As the FCNN input, the UCAE consistently outperformed the UCFS, achieving R^2 values of approximately 0.99 for both E_x and E_y , with a mean absolute error of about 1.4 MPa. Based on the FE database, a k-nearest neighbors strategy was applied to retrieve the five structures most closely matching the target modulus. The selected designs were subsequently fabricated by high-precision 3D printing. The elastic modulus values obtained from machine learning prediction, finite element analysis, and experimental testing showed close agreement. Overall, this framework enables rapid prediction and inverse screening of elastic modulus in ET-based structures with high degrees of freedom.

*Corresponding authors:

Xing Zhang
(xingzhang@imr.ac.cn)
Deliang Zhang
(zhangdeliang@mail.neu.edu.cn)

Citation: Wu Z, Dong X, Cao L, Zhang D, Zhang X. Machine learning-enabled prediction and inverse screening of elastic modulus in Euclidean-tiling structures. *Int J AI Mater Design*. 2026;3(1):94-109.
doi: 10.36922/IJAMD026060001

Received: February 8, 2026

Revised: March 11, 2026

Accepted: March 18, 2026

Published online: March 27, 2026

Copyright: © 2026 Author(s). This is an Open-Access article distributed under the terms of the Creative Commons Attribution License, permitting distribution, and reproduction in any medium, provided the original work is properly cited.

Publisher's Note: AccScience Publishing remains neutral with regard to jurisdictional claims in published maps and institutional affiliations.

Keywords: Fully connected neural network; K-nearest neighbors; 3D printing

1. Introduction

A key objective in structural design of the orthopedic implant is to achieve appropriate mechanical matching between the implant and the host bone while satisfying load-bearing requirements, thereby reducing stress shielding and extending the service life of the implant.^{1,2} The elastic modulus of natural bone is known to vary widely, with cancellous bone typically exhibiting an elastic modulus of tens of MPa, while cortical

bone can reach several GPa.³⁻⁸ When load bearing is dominated by the intrinsically high stiffness of the implant material, stress transfer to the surrounding bone is substantially reduced, leading to stress shielding and subsequent bone resorption. This process may ultimately result in interfacial debonding, implant loosening, and mechanical failure.⁹⁻¹¹ Accordingly, modulating the elastic modulus of orthopedic implants through geometric architecture, rather than relying solely on bulk material properties, has emerged as a critical design strategy in scaffold and implant engineering.¹²

In this context, porous and lattice scaffolds have been extensively employed in bone repair and bone substitute design, as low density, high specific strength, high specific stiffness, and broad tunability of porosity and topology can be achieved through architectural design.¹³ For instance, a systematic review of additively manufactured porous metallic scaffolds for bone tissue engineering summarized their mechanical and biological behavior and indicated that the effective elastic modulus could be continuously tuned within the range of 0.1–10 GPa through unit cell level topological design.¹⁴ A further review on 3D-printed porous ceramics and ceramic-based composite scaffolds highlighted that pore size, interconnectivity, and anisotropy collectively govern bone ingrowth and mechanical matching.¹⁵ In addition, a topology-oriented assessment of multiscale lattice architectures discussed their application potential in lightweight and biomedical engineering.¹⁶ Nevertheless, much of the existing literature has been built upon regular honeycombs, triply periodic minimal surface (TPMS)-based lattices, or a limited number of representative unit cells.¹⁷ In many existing studies, the elastic modulus is modulated principally by altering porosity, cellular scale, strut, or wall thickness. Regulation of these parameters tends to produce relatively monotonous overall structures, thereby limiting the tunable range of elastic modulus.

To further expand the accessible design space, increasing attention has been directed toward bioinspired aperiodic architectures and irregular tiling structures.¹⁸ Irregular architected materials inspired by natural tissues have been constructed using virtual growth rules, through which short-range order and long-range aperiodicity can be achieved, enabling directional regulation of stress distribution and improved load support performance.¹⁹ In subsequent developments, an adjacency rule-guided, virtual growth-based topology optimization framework for irregular multiscale architectures was established by integrating adjacency constraints with multiscale optimization strategies. Within this framework, multiple irregular configurations were generated to match

prescribed target stress fields and effective stiffness distributions.²⁰ In addition, foundational studies on Euclidean-tiling (ET) systematically classified and enumerated seamless planar tilings, demonstrating that many tiling patterns can be formed using a finite set of regular or semiregular polygons.²¹⁻²³ Finite element analysis (FEA) investigations on stochastic and irregular unit cells have further demonstrated that cell shape disorder and wall thickness variability can significantly alter effective stiffness and crushing responses, while also modifying the degree of directional sensitivity. For example, Voronoi-based imperfect honeycombs have been shown to exhibit systematic variations in elastic modulus and crushing or plateau behavior with increasing geometric irregularity.²⁴⁻²⁶ However, classical ET are defined by strict geometric and combinatorial constraints. As a result, the number of ET-families remains finite and has been largely enumerated in the mathematical literature, which limits the scalability of ET-based database when continuously expandable and learning-ready structural libraries are desired.^{21,27}

Following the rapid growth of architectural complexity, increasing importance has been attributed to data-driven surrogate modeling for structure-property prediction and inverse design in architected materials. The need for repeated high-fidelity simulations can be substantially reduced through machine learning (ML) frameworks when high-dimensional design spaces are explored.²⁸ Recent generative and inverse design studies have further demonstrated efficient retrieval and synthesis of architectures that match prescribed mechanical responses.²⁹⁻³¹ In addition, ML-based image and voxel representations have enabled the prediction of stress and strain directly from microstructural information.^{32,33} Alternative effective representations are provided by graph-based approaches, through which connectivity and topology in truss and lattice metamaterials can be encoded to support property prediction and design space exploration.³⁴⁻³⁸ Currently, limited research has applied ML to regulate mechanical properties, such as elastic modulus, through structural design in biomaterial-based bone implants, thereby motivating the present work.

In this work, a data-driven framework is proposed for programmable ET structures, aiming to expand geometric freedom while enabling controllable in-plane mechanical behavior. The primary contribution of the present study lies in establishing a programmable ET-based geometric design space for multi cell structures and a data-driven framework for regulating in-plane elastic modulus in the context of orthopedic implants. Based on a set of tiling-compatible unit cells including tris, quad, and oct, large ensembles of irregular multicell tiling structures are

generated through random assembly, and their structure property relationships are systematically characterized using homogenized FEA. To support efficient surrogate modeling, alternative feature representations are introduced to encode architectural information, and a neural network-based predictor is established for rapid estimation of effective in-plane elastic modulus. Building on the resulting structure-property database, an inverse screening strategy is further implemented to retrieve candidate architectures that satisfy prescribed target elastic modulus. The feasibility of the proposed framework is validated experimentally through 3D printing and mechanical testing, demonstrating close agreement with numerical predictions.

2. Methods

The programmable ET structures constructed enable continuous tuning of in-plane mechanical properties through the diversified combination of geometric units. A complete data-driven design framework of integrating structure generation, performance simulation, ML prediction, and inverse screening was established to systematically quantify the influence of different tiling combinations on in-plane modulus (E_x and E_y) and verify

the prediction reliability of machine learning models. The overall research framework is shown in Figure 1.

2.1. Structure generation and geometric modeling

For the construction of programmable ET structures, the representation of the basic unit cells must first be defined to ensure geometric consistency and topological compatibility during subsequent random assembly and FEA. Initially, eight candidate unit cells were designed, and their corresponding pixel representations were generated, as shown in Figure 2A. During the subsequent node and element representation stage, several candidates were excluded due to geometric incompatibility or the inability to achieve seamless planar tiling (Figure 2B). Ultimately, three basic unit cells, denoted as tris, quads, and oct, were retained, as these units support seamless tiling within a unit domain while exhibiting distinct geometric characteristics and mutual combinability (Figure 2C). Based on these three unit cells, a 5×5 structural ensemble was generated through random tiling. As a result, complex planar configurations comprising triangles, quadrilaterals, pentagons, hexagons, and octagons were obtained, effectively capturing the geometric diversity inherent to ET (Figure 2D).

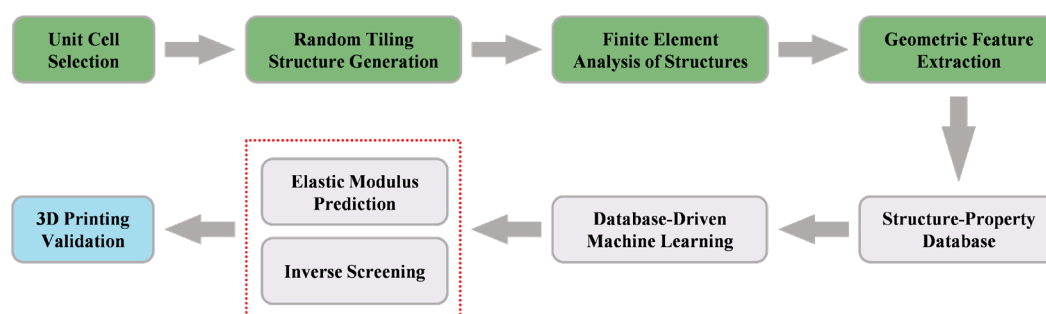


Figure 1. Schematic of elastic modulus prediction and inverse screening of Euclidean-tiling (ET) structure based on machine learning

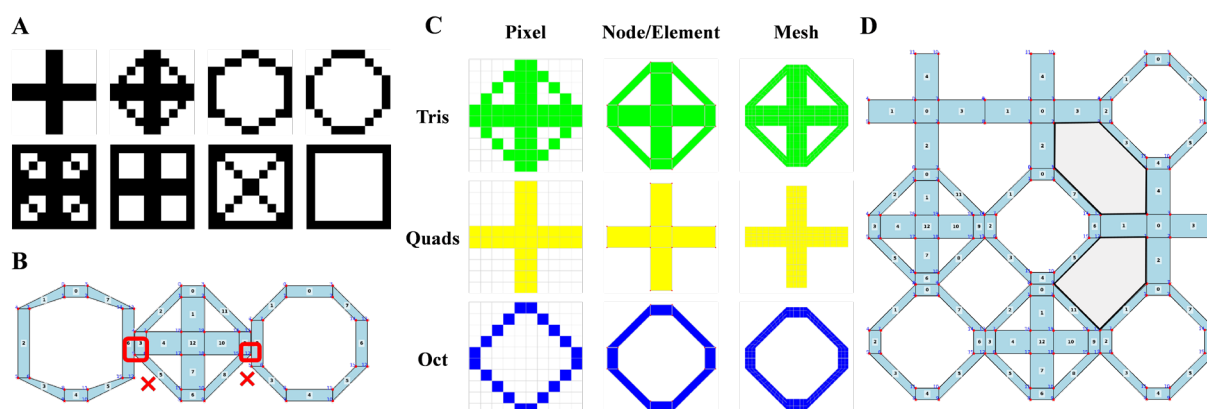


Figure 2. Unit cell selection: (A) alternative unit cells, (B) invalid combination, (C) selected unit cells, (D) effective combination

After the construction of the basic unit cells, a virtual growth algorithm based on adjacency rules is adopted to enable the automated generation of structures.³⁹ By integrating geometric compatibility constraints within local neighbors with global frequency regulation, the algorithm progressively fills the entire structural domain. Through this process, tiling structures with high geometric degrees of freedom can be generated while preserving short-range order and long-range aperiodicity. As a result, complex aperiodic structures satisfying strict geometric constraints are efficiently produced, providing high quality structures for subsequent FEA and data-driven modeling.

2.2. Finite element analysis and database construction

To enable accurate mapping between geometric features and elastic modulus, FEA is employed to numerically evaluate a wide range of programmable ET structures. The corresponding in-plane elastic modulus (E_x and E_y) are extracted, and a high-throughput structure property database is thereby constructed. Three representations of the overall structural model (pixel, node/element, and mesh) are illustrated in Figure 3.

In numerical modeling, the plane stress assumption is adopted for two-dimensional (2D) cell units, and finite element models are established based on four-node Q4 elements. Periodic boundary conditions are imposed on the geometric boundaries of each unit cell to ensure consistent displacements and strains of nodes on opposite boundaries. A typical mesh is divided into 5×5 elements with a constant thickness ($t = 1$). The constitutive material parameters used in FEA are illustrated in Figure S1. They are determined from uniaxial compression tests on three bulk resin cylinders under the same conditions as those described in the main text. Based on the stress-strain curves in the 2–5% strain range, the average elastic

modulus is determined to be approximately 640 MPa. To simulate the weakening effect of the void space on the mechanical response, the material parameters adopt equivalent linear elastic constants, in which E_s represents the elastic modulus of the solid phase, and E_v represents the equivalent elastic modulus assigned to the void phase, with $E_v = 0.001 E_s$ and Poisson's ratio $\nu = 0.1$.

During the solution procedure, periodic boundary decomposition is first applied to the nodal displacement field of the unit cell. The periodic vectors of the microstructure are set as \mathbf{a}_1 , \mathbf{a}_2 and the total node displacement \mathbf{d} can be decomposed into the sum of the free displacement \mathbf{d}_0 and the periodic boundary additional displacement $\Delta \mathbf{a}$:

$$\mathbf{d} = \mathbf{B}_0 \mathbf{d}_0 + \mathbf{B}_a \Delta \mathbf{a} \quad (1)$$

where \mathbf{B}_0 and \mathbf{B}_a are the topological matrices of independent and dependent degrees of freedom, respectively. Combining these with the global stiffness matrix \mathbf{K}_{uc} , the periodic equilibrium equation is established:

$$\mathbf{B}_0^T \mathbf{K}_{uc} \mathbf{d}_0 = 0 \quad (2)$$

The relational expression between free displacement and boundary displacement is solved:

$$\mathbf{D} = \mathbf{D}_a \Delta \mathbf{a}, \mathbf{D}_a = \mathbf{B}_0 \mathbf{D}_0 + \mathbf{B}_a \quad (3)$$

Here, \mathbf{D}_0 is the influence matrix relating the free displacement to the imposed boundary displacement, and \mathbf{D}_a is the global transformation matrix relating the periodic boundary additional displacement $\Delta \mathbf{a}$ to the total nodal displacement \mathbf{d} .

The macroscopic equivalent stiffness matrix is further calculated through the principle of energy equivalence:

$$\mathbf{K}_e = \frac{1}{V} \mathbf{B}_e^T \mathbf{K}_{\Delta a} \mathbf{B}_e \quad (4)$$

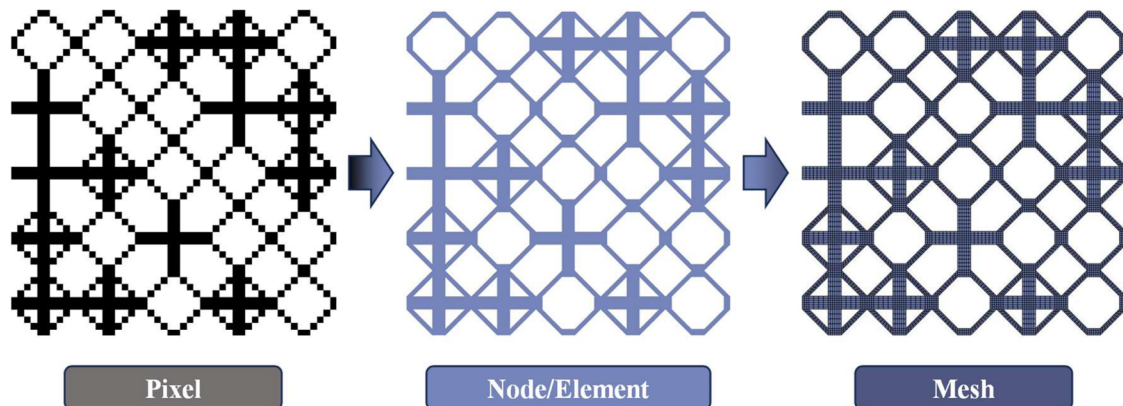


Figure 3. Three representation forms of the programmable structure

where V represents the unit cell volume, \mathbf{B}_ε denotes the strain-displacement relationship matrix, and $\mathbf{K}_{\Delta a} = \mathbf{D}_a^T \mathbf{K}_{uc} \mathbf{D}_a$ corresponds to the equivalent stiffness matrix for macroscopic deformation.

Constitutive stiffness matrix under 2D plane stress conditions is typically expressed as:

$$\mathbf{K}_\varepsilon = \begin{bmatrix} C_{11} & C_{12} & C_{13} \\ C_{21} & C_{22} & C_{23} \\ C_{31} & C_{32} & C_{33} \end{bmatrix}. \quad (5)$$

The constitutive coefficients C_{ij} ($i, j = 1, 2, 3$) denote the components of the equivalent stiffness matrix under 2D plane stress conditions, where C_{11} and C_{22} correspond to the normal stiffness in the x and y directions, respectively, and C_{22} represents the coupling stiffness between the two in plane directions. Under the assumption of orthotropic anisotropy ($C_{13} \approx C_{23} \approx 0$), the components satisfy the following relationship with the equivalent elastic constants:

$$C_{11} = \frac{E_x}{1 - \nu_{xy}\nu_{yx}}, \quad C_{22} = \frac{E_y}{1 - \nu_{xy}\nu_{yx}}, \quad C_{12} = \frac{\nu_{yx}E_x}{1 - \nu_{xy}\nu_{yx}} = \frac{\nu_{xy}E_y}{1 - \nu_{xy}\nu_{yx}}$$

where the reciprocity condition $\nu_{xy}/E_y = \nu_{yx}/E_x$ holds universally.

Therefore, the equivalent elastic modulus can be inversely calculated from the components in \mathbf{K}_ε :

$$E_x = C_{11}(1 - \nu_{xy}\nu_{yx}), \quad (6)$$

$$E_y = C_{22}(1 - \nu_{xy}\nu_{yx}). \quad (7)$$

Considering that the Poisson's ratio of the 2D programmable ET structures studied in this paper is small ($\nu \approx 0.1$), the influence of transverse strain on the principal stress direction is limited.⁴⁰ Meanwhile, since $1 - \nu_{xy}\nu_{yx} \approx 0.99$, $E_x \approx C_{11}$, $E_y \approx C_{22}$ are adopted as suitable approximations. With relative errors below 1%, C_{11} and C_{22} are used as representative parameters for the equivalent in-plane elastic modulus E_x and E_y , facilitating efficient performance characterization and ML model training.

2.3. Machine learning modeling and inverse screening

2.3.1. Feature representation and standardization

Based on the structure-property database obtained from FEA, two types of geometric feature input forms are constructed in this study. One is nit cell arrangement encoding (UCAE), which expands the 5×5 structure into a 25-dimensional encoding vector $\mathbf{X} \in \{3, 4, 8\}^{25}$, where 3, 4, and 8 correspond to the three unit cell types (tris, quads, oct), respectively. The other is unit cell frequency statistic (UCFS), which records the

proportion of the three types of unit cells in the structure

$$\mathbf{x} = [f_{\text{tris}}, f_{\text{quads}}, f_{\text{oct}}], f_{\text{tris}} + f_{\text{quads}} + f_{\text{oct}} = 1.$$

The output variable is a 2D target vector $\mathbf{y} = [E_x, E_y]$, representing the equivalent elastic modulus in the two principal in-plane directions, respectively.

Due to the large difference in dimensions between various features, direct training leads to gradient imbalance and unstable convergence. Thus, both input and output data are standardized to transform each dimension feature into a zero-mean, unit-variance form:

$$\tilde{\mathbf{x}} = \frac{\mathbf{x} - \boldsymbol{\mu}_x}{\boldsymbol{\sigma}_x}, \quad \tilde{\mathbf{y}} = \frac{\mathbf{y} - \boldsymbol{\mu}_y}{\boldsymbol{\sigma}_y} \quad (8)$$

where $\boldsymbol{\mu}$ and $\boldsymbol{\sigma}$ are the sample mean and standard deviation, respectively. After prediction, the original dimension is restored through inverse standardization:

$$\hat{\mathbf{y}} = \boldsymbol{\mu}_y + \tilde{\mathbf{y}} \odot \boldsymbol{\sigma}_y \quad (9)$$

This processing ensures that input features under different dimensions have the same numerical weight during training, thereby accelerating convergence and improving model stability.

2.3.2. Network architecture and activation function

The model adopts a three-layer fully connected neural network (FCNN). The input layer dimension is determined by the feature type (25 or 3), and the output layer corresponds to (E_x, E_y) . The number of neurons in the two hidden layers is $m, p \in \{8, 16, 32, 64, 128, 256, 512\}$, and the optimal combination is determined through hyperparameter search.

The forward propagation relationship of the network is:

$$\begin{aligned} \mathbf{h}_1 &= \text{ReLU}(\mathbf{W}_1 \tilde{\mathbf{x}} + \mathbf{b}_1) \\ \mathbf{h}_2 &= \text{ReLU}(\mathbf{W}_2 \mathbf{h}_1 + \mathbf{b}_2) \\ \tilde{\mathbf{y}}_{\text{pred}} &= \mathbf{W}_3 \mathbf{h}_2 + \mathbf{b}_3 \end{aligned} \quad (10)$$

where \mathbf{W}_i and \mathbf{b}_i ($i = 1, 2, 3$) represent the weight and bias parameters, respectively.

The activation function employs ReLU (rectified linear unit), defined as:

$$\text{ReLU}(z) = \max(0, z) \quad (11)$$

This function offers strong nonlinear representation capability, computational simplicity, and avoids gradient vanishing.

2.3.3. Loss function and optimization strategy

The network training objective is to minimize the mean squared error (MSE) between predicted and actual values:

$$L(\Theta) = \frac{1}{N} \sum_{i=1}^N \|\tilde{\mathbf{y}}_{\text{pred}}^{(i)} - \tilde{\mathbf{y}}^{(i)}\|_2^2 \quad (12)$$

where Θ denotes the set of network parameters and N represents the total number of samples.

An Adam optimizer (adaptive moment estimation) is adopted, in which the learning rate is adaptively adjusted using first- and second-order gradient moment estimates. The parameter update equations are expressed as:

$$\begin{aligned} m_t &= \beta_1 m_{t-1} + (1 - \beta_1) g_t \\ v_t &= \beta_2 v_{t-1} + (1 - \beta_2) g_t^2 \\ \hat{m}_t &= \frac{m_t}{1 - \beta_1^t}, v_t = \frac{v_t}{1 - \beta_2^t} \\ \theta_t &= \theta_{t-1} - \eta \frac{\hat{m}_t}{\sqrt{\hat{v}_t} + \varepsilon} \end{aligned} \quad (13)$$

where g_t is the gradient, and η is the learning rate, and the parameters are set as $\beta_1 = 0.9$, $\beta_2 = 0.999$, and $\varepsilon = 10^{-8}$.

To ensure training stability and efficiency, a multi-level learning rate scheduling and early stopping mechanism are adopted.⁴¹ In addition, inputs and outputs are uniformly standardized to ensure balanced contributions of different physical quantities to gradients, thereby achieving a stable and efficient optimization process.

2.3.4. Data splitting and K-fold cross validation

Sample data are divided into a training validation set (85%) and an independent test set (15%), and the random seed is fixed to ensure reproducibility. During the training phase, 5-fold cross validation is adopted for the training-validation set, and the minimum value of the validation set loss is:

$$\text{ValLoss}_{\min} = \min_t \text{ValLoss}^{(k)}(t) \quad (14)$$

The mean and standard deviation are calculated:

$$\mu_{\text{CV}} = \frac{1}{5} \sum_{k=1}^5 \text{ValLoss}_{\min}^{(k)} \quad (15)$$

$$\sigma_{\text{CV}} = \sqrt{\frac{1}{5} \sum_{k=1}^5 (\text{ValLoss}_{\min}^{(k)} - \mu_{\text{CV}})^2} \quad (16)$$

The average validation error μ_{CV} reflects the overall accuracy of the model, and the standard deviation σ_{CV} measures the stability of the model under different splits. Training results (including loss curves, model size, and time consumption) of all configurations (μ, m, p) are saved. The top five optimal configurations with the smallest average validation error, smallest standard deviation, least

number of parameters, and shortest calculation time are finally retained as candidates.

2.3.5. Inverse screening via KNN

To realize rapid inverse search of target properties, the k-nearest neighbors (KNN) algorithm is introduced based on the trained database in this study.⁴² Given the expected performance target: $\mathbf{y}^* = [E_x^*, E_y^*]$.

The Euclidean distance between each sample performance point $\mathbf{y}_i = [E_{x,i}, E_{y,i}]$ in the sample database and the target point is calculated:

$$d_i = \sqrt{(E_x^* - E_{x,i})^2 + (E_y^* - E_{y,i})^2} \quad (17)$$

The K samples with the smallest distances $\{\mathbf{y}_{i_1}, \dots, \mathbf{y}_{i_K}\}$ are selected, and the corresponding structural parameters $\{\mathbf{x}_{i_1}, \dots, \mathbf{x}_{i_K}\}$ are output as candidate structures meeting the target performance.

The inversion accuracy is evaluated by mean absolute error (MAE) and relative error (RE):

$$\text{MAE} = \frac{|E_x(\hat{\mathbf{x}}) - E_x^*| + |E_y(\hat{\mathbf{x}}) - E_y^*|}{2} \quad (18)$$

$$\text{RE} = \frac{|E_x(\hat{\mathbf{x}}) - E_x^*|}{E_x^*} + \frac{|E_y(\hat{\mathbf{x}}) - E_y^*|}{E_y^*} \quad (19)$$

2.4. Fabrication of 3D printing samples and compression tests

To validate the manufacturability of the programmable ET structures and the mechanical validity of the numerical predictions, several representative structures were selected and fabricated by 3D printing. The in-plane elastic modulus of the printed samples was obtained and compared with FEA and ML. The experimental workflow comprised thickness assignment and STL generation from 2D meshes, micro-scale 3D printing, post-processing and geometric inspection, and compression tests.

2.4.1. Thickness assignment of 2D meshes and model generation

Based on the 2D mesh files (.npz) generated in the FEA, node coordinates and element connectivity were first imported and processed using a custom Python script. A second layer of nodes was created by duplicating the original nodes along the thickness direction (z-axis) to form the top surface. A uniform nominal thickness of $t = 2.0$ was adopted for all samples, corresponding to the printable structures. A 3D nodal set including bottom and top

layers was constructed. Following thickness assignment, each planar element was triangulated to form the bottom and top surfaces, with additional facets defining the four lateral sidewalls. All facets were assembled into a standard STL triangulated surface, and an individual STL file was exported for each structure to serve as the geometric input for subsequent 3D printing.

2.4.2. Micro-scale photopolymerization 3D printing

The generated STL models were imported into Materialise Magics (Materialise, Belgium) for mesh repair and topological inspection. Specifically, duplicate and degenerate facets were removed, holes and non-manifold boundaries were repaired, and self-intersections as well as disconnected faces were checked to ensure that the models constituted closed and printable solids. Slicing was then performed in Magics with a layer thickness of 20 μm .

Fabrication was carried out using a BMF NanoArch[®] S130 micro-precision lithography printer operating on projection micro-stereolithography. The pixel size was approximately 2 μm , and the achievable layer thickness ranged from 5 to 20 μm , which satisfied the feature-resolution requirements of the programable ET structures considered in this study. A commercial BIO photopolymer resin supplied by BMF (China) was used as the printing material. Owing to the high crosslinking density after curing and favorable biocompatibility, the resin was considered suitable as a structural carrier within the proposed samples. Detailed printing parameters were provided in Table S1, including the number of layers, light intensity, exposure time, layer thickness, and settling time for each layer. Longer exposure times were used in the initial layers to improve curing and adhesion to the printing platform. The settling time, defined as the pre-exposure resin leveling period, was gradually shortened during the printing process.

After printing, samples were removed from the printing platform and cleaned in isopropanol using ultrasonication to eliminate uncured resin. Post-curing was subsequently performed under a 405 nm ultraviolet source for 5 min to ensure complete curing and dimensional stability prior to optical inspection and mechanical testing.

2.4.3. Geometric verification and loading-direction registration

Representative samples were evaluated by optical microscopy to confirm geometric accuracy of the designed tiling structure. Images were acquired to verify the connectivity of the intended unit cells and to inspect the thickness and corners. The printed geometries were compared with the meshes in terms of nodal distribution,

boundary contours, and the shapes of cell connections. Particular attention was paid to whether tiling boundaries were closed, whether fractured or missing features occurred, whether the internal voids retained the intended tris, quads, and oct characteristics, and whether the overall 5×5 arrangement was consistent with the numerical designs. After passing geometric inspection, the loading directions were registered and marked on the samples in the testing fixtures, such that the horizontal and vertical compression directions corresponded to E_x and E_y , respectively, as defined in the FEA and ML.

2.4.4. Compression tests and determination of elastic modulus

Compression tests were conducted on a uniaxial micro-mechanical testing system under displacement control using a compression fixture. For each representative tessellation, at least $n \geq 3$ samples were fabricated and tested, and compression was performed along both the x and y directions to obtain direction-dependent effective modulus. A loading rate of $\nu = 0.5 \text{ mm/min}$ was used, corresponding to an effective strain rate of approximately $1.67 \times 10^{-3} \text{ s}^{-1}$ after scaling by sample dimensions, therefore inertial and viscous effects were minimized and quasi-static conditions were approximated. Load-displacement data (F , ΔL) were recorded continuously during testing. Using the initial cross-sectional area A_0 and the initial height L_0 , the nominal stress and engineering strain were calculated as: $\sigma = \frac{F}{A_0}$, $\epsilon = \frac{\Delta L}{L_0}$.

The initial linear segment of each stress-strain curve, typically within $\epsilon \in [0.2\%, 1.0\%]$ or selected according to the curve morphology, was fitted by least-squares linear regression, and the slope was taken as the experimental effective elastic modulus in the corresponding loading direction. For each structure and loading direction, the mean and standard deviation were computed from at least three repeated tests to obtain representative elastic modulus in both directions.

3. Results and discussion

3.1. FCNN model for modulus prediction

3.1.1. Hyperparameter selection and optimal configuration

To obtain a stable and high accuracy prediction model, systematic hyperparameter traversal and screening were conducted on two types of input features, namely UCAE and UCFS. The learning rate range was set as $\{10^{-5}, 10^{-4}, 10^{-3}, 10^{-2}, 10^{-1}\}$ and the number of hidden layer nodes included 8, 16, 32, 64, 128, 256, 512. Candidate configuration sets were formed through traversal of two

hidden layer combinations. All candidate models were evaluated for robustness using 5-fold cross validation ($K = 5$), and optimized based on the mean and variance of validation errors.

Finally, the UCAE model achieved the best performance under the parameter combination [$LR = 1 \times 10^{-3}$, $m = 128$, $p = 64$], while the optimal combination for the UCFS model was [$LR = 1 \times 10^{-3}$, $m = 64$, $p = 16$]. Comparison of global indicators showed that the validation MSE of the UCAE model is approximately one-third of that of the UCFS model, and the validation standard deviation was significantly lower, indicating higher generalization consistency across different data folds. For transparency, Figure S2 summarizes the selected hyperparameter settings together with the weight matrix heatmaps and bias distributions of the three fully connected layers for the UCAE and UCFS models. Compared with the UCFS model, the UCAE model exhibits more structured and regular weight patterns across layers, consistent with its stronger ability to capture nonlinear relationships associated with complex topological features and multidimensional geometric patterns, whereas the UCFS model shows less structured weight distributions, suggesting a greater reliance on global average fitting under limited input information.

Based on the loss curves (Figure 4) of the two input models under their respective optimal parameter settings, both models converged rapidly within the first 10 training epochs. For the UCAE-based model, the training and validation errors almost completely overlapped and ultimately decreased to an MSE below 0.01, indicating stable network convergence without evident overfitting. In contrast, the validation loss of the UCFS-based model

remained substantially higher than the corresponding training loss and stabilized at approximately an MSE of 0.04, suggesting information loss and underfitting associated with the low-dimensional input representation. From an algorithmic perspective, these results indicate that the UCAE input preserves more complete geometric information, enabling the network to learn complex nonlinear structure-property mappings. Consequently, rapid and stable convergence can be achieved even with a limited number of training samples, thereby providing a solid basis for prediction accuracy analysis.

3.1.2. Comparative analysis of prediction accuracy and error

To further evaluate the accuracy and predictive performance of the two models in elastic modulus, the prediction results and error distributions of the UCAE and UCFS models were analyzed on the test database. As shown in Figure 5A,B, the scatter points comparing the predicted and true values of E_x and E_y of both models were largely distributed along the diagonal, indicating overall predictive consistency. However, the UCAE-based model exhibited a higher goodness of fit and a more compact point cloud distribution. The associated error distributions (Figure 5C,D) further revealed that the prediction errors of the UCAE-based model were strongly concentrated around zero, forming a sharp-peak and narrow-band distribution, with most absolute errors remaining within ± 5 . In contrast, the UCFS-based model displayed a significantly broader error distribution with pronounced long-tailed characteristics, indicating substantial prediction deviations for a subset of samples.

Quantitative error statistics further demonstrated clear

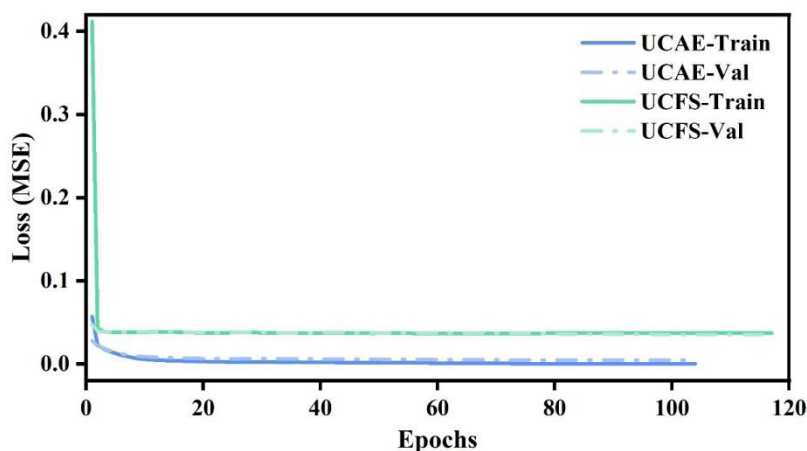


Figure 4. Training and validation loss convergence of FCNN models with UCAE and UCFS inputs under their optimal hyperparameters. Abbreviations: FCNN: Fully connected neural network; MSE: Mean squared error; UCAE: Unit cell arrangement encoding; UCFS: Unit cell frequency statistic.

performance differences between the two models (Figure 6). An integrated comparison of predictive accuracy and computational cost was further obtained using radar-chart visualization (Figure 6A). The triangular radar representation jointly summarized the training time and the test-set coefficients of determination along both principal directions. Compared with the UCFS model ($R_{E_x}^2 = 0.962$ and $R_{E_y}^2 = 0.963$), the UCAE model exhibited substantially higher goodness-of-fit in both directions ($R_{E_x}^2 = 0.989$ and $R_{E_y}^2 = 0.994$), although it required a moderately longer training time. The larger enclosed area along the axes reflected a consistently stronger predictive capability, achieved with only a limited increase in computational expense. Error-related performance metrics were further compared using a five-axis radar chart (Figure 6B).

Considering the MAE and root mean square error (RMSE) for both E_x and E_y together with the cross-validation error, the UCAE model formed a markedly more compact polygon, indicating consistently lower

errors and improved numerical stability. Correspondingly, the MAE of the UCAE model were 1.37 MPa and 1.36 MPa for the predicted elastic modulus E_x and E_y , respectively, which were markedly lower than those of the UCFS model (3.67 MPa and 3.57 MPa, respectively). A similar trend was observed for the mean squared error metric, where the cross-validation MSE of the UCAE model reached only 0.005, compared with that for the UCFS model (0.037). Consistently lower cross-validation MSE values further confirmed superior robustness across different data splits. In summary, the radar chart demonstrates that UCAE exhibits superior predictive capabilities and the capacity for generalization when compared with UCFS.

3.2. KNN-based inverse screening

To assess the feasibility of inverse design based on the structure-property database, a target performance point

$E_x^* = E_y^* = 100$ MPa was selected as a representative example, and a standardized KNN algorithm was employed to perform inverse retrieval in the performance

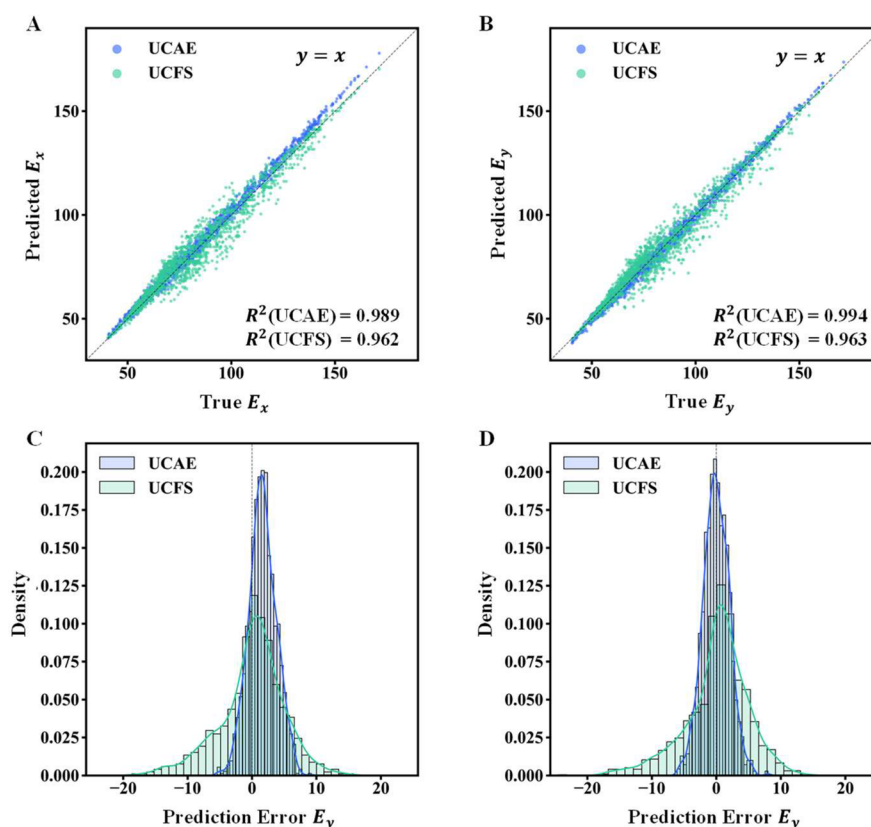


Figure 5. Prediction accuracy and error distributions for in-plane modulus: (A) E_x prediction accuracy, (B) E_y prediction accuracy, (C) prediction error distribution for E_x , (D) prediction error distribution for E_y .

Abbreviations: UCAE: Unit cell arrangement encoding; UCFS: Unit cell frequency statistic.

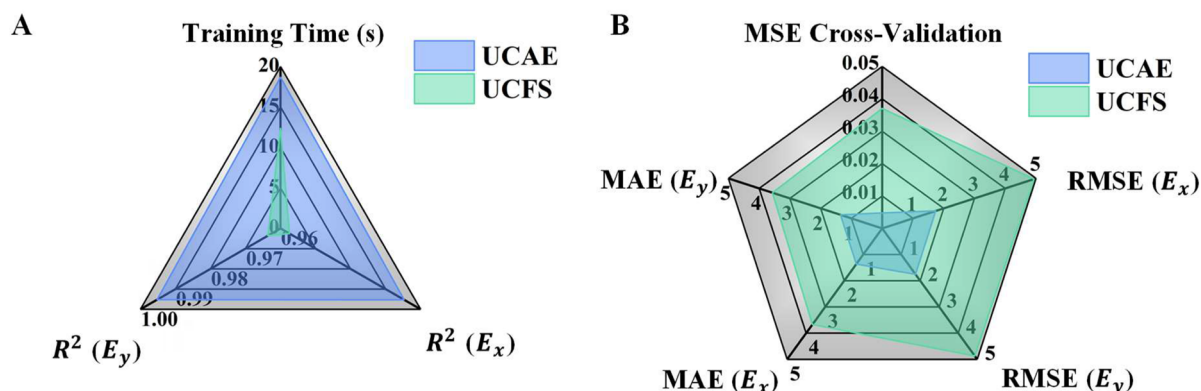


Figure 6. Radar-chart comparison of predictive performance between UCAE and UCFS models. (A) Training time and test-set R^2 in the E_x and E_y directions; (B) Error statistics including MAE (E_x and E_y), RMSE (E_x and E_y), and cross-validation MSE.

Abbreviations: MAE: Mean absolute error; MSE: Mean squared error; RMSE: Root mean square error; UCAE: Unit cell arrangement encoding; UCFS: Unit cell frequency statistic.

space. By examining the performance distribution, error symmetry, and distance statistics of neighboring samples, the accuracy and stability of the inverse screening process, as well as the local density characteristics of the database, were systematically evaluated. The corresponding results are presented in Figure 7.

A dominant distribution trend was observed along the $E_x = E_y$ diagonal in the E_x and E_y performance space, indicating pronounced covariation of the in-plane elastic modulus across the design space (Figure 7A). The selected target point was located within this dominant band, and the corresponding KNN neighbors clustered tightly around the target at the global scale, suggesting that the target resided in a densely sampled and readily accessible region of the database. A local magnified view within a ± 2 MPa window further revealed that the neighboring samples were symmetrically distributed around the target without noticeable one-sided clustering or pronounced deviation, indicating locally continuous behavior of the performance space and limited directional distortion in the immediate vicinity (Figure 7B). Such characteristics support stable and reproducible inverse screening.

The influence of neighbor size on inverse screening error was examined by analyzing the variation of MAE and RMSE with respect to the sample index. Both error metrics increased monotonically and exhibited progressively smoother trends as the sample index grew, indicating that local similarity was gradually diluted when more distant neighbors were incorporated and that the error transitioned from a local optimum toward a global average (Figure 7C). This behavior reflected a characteristic scale trade-off in KNN-based inversion, in which smaller neighbors preserved local consistency, whereas larger neighbors

increasingly included samples with greater mismatch to the target. A magnified view of the first five nearest neighbors further showed that both MAE and RMSE remained low and increased only gradually within this range, indicating that performance deviations were well controlled among the closest candidate set and that the neighbor ranking was consistent with the observed error evolution (Figure 7D). When considered together with the symmetric local distribution observed previously, these results suggested that inverse screening with a small neighbor size achieves a practical balance between prediction accuracy and candidate diversity.

Beyond error-based metrics, distance statistics were employed to characterize the local database density around the target from a geometric perspective. The distribution of distances between the target and all database samples, together with the corresponding cumulative percentage, exhibited a unimodal profile with a high frequency at small distances, indicating continuous and well-covered sampling of the performance space (Figure 7E). A closer examination of the local neighbor further revealed that the distances associated with the first five nearest neighbors all remained below 0.02 mm and were primarily clustered around approximately 0.01 mm, demonstrating a compact and high-density local region surrounding the target (Figure 7F). Such distance characteristics provided direct evidence of sufficient local sampling density, thereby supporting high precision and stable inverse screening.

Taken together, the inverse retrieval results targeting E_x and E_y demonstrated that KNN consistently identified a dense local neighbor around the target within the globally dominant performance band, yielding a compact candidate set characterized by locally symmetric placement

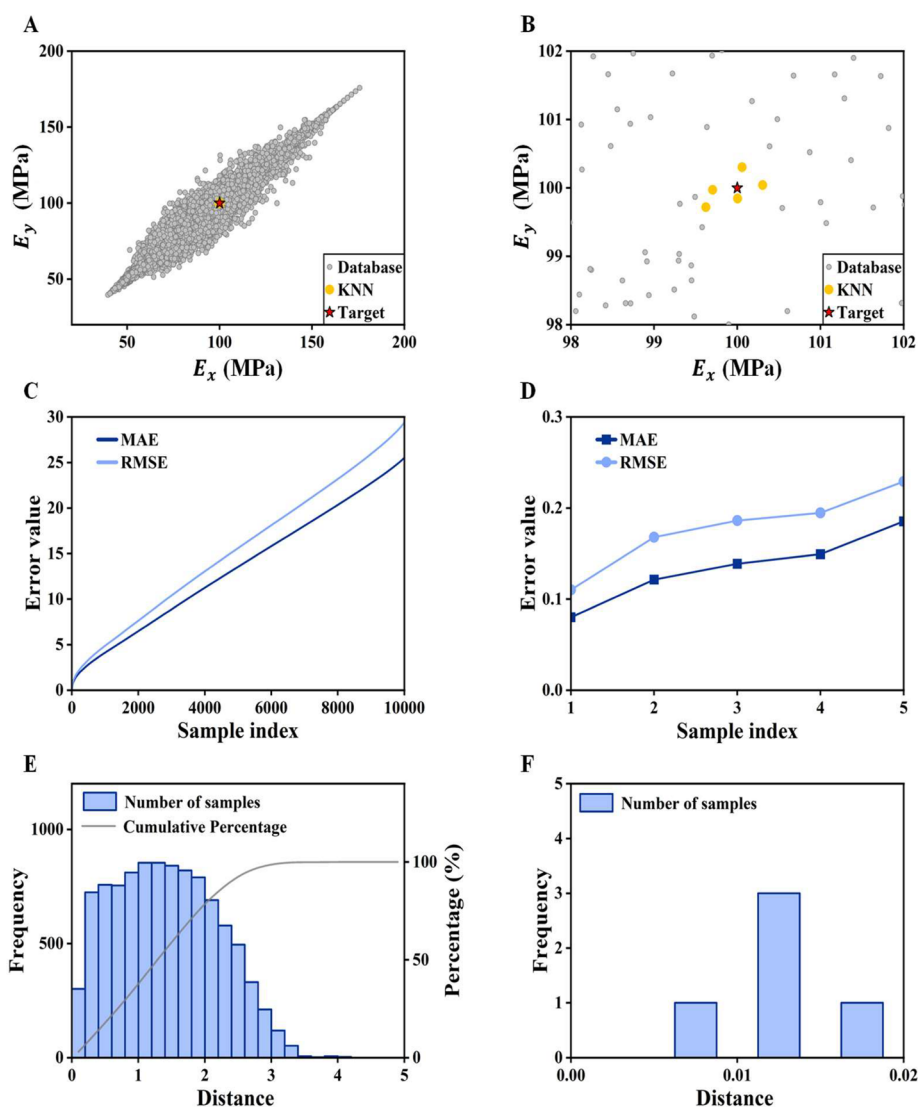


Figure 7. KNN-based inverse screening in the E_x and E_y space and neighbor statistics. (A) global E_x and E_y performance map showing the target and KNN-selected neighbors, (B) zoomed local neighbor within ± 2 MPa around the target, (C) MAE and RMSE as functions of the neighbor rank (sample index) over the full database (1–10,000), (D) enlarged view of MAE and RMSE for the top-5 neighbors, (E) distance distribution from the target to all database samples with the cumulative percentage, (F) distance histogram of the top-5 KNN neighbors.

Abbreviations: KNN: K-nearest neighbors; MAE: Mean absolute error; RMSE: Root mean square error.

and small inter-sample distances (Figure 7). In addition, the systematic increase in prediction error with neighbor expansion indicated that smaller neighbor sizes were more effective in preserving local consistency and inversion accuracy. These observations support the use of relatively small K values for reliable and accurate inverse screening.

3.3. 3D printing samples and compression tests

Photographs of the five printed samples and their corresponding numerical models demonstrated high-fidelity reproduction of the designed structures across all

configurations (Figure 8). The spatial distributions and connectivity of tris, quads, and oct cells were consistently preserved, with no apparent macroscopic distortions or missing features. At the microscale, the printed geometries remained in close agreement with the designed models, with the measured dimensional deviation being within 10 μm for a nominal strut diameter of approximately 300 μm . Relative density is also an important factor affecting elastic modulus. However, in the present ET design, the geometric and connection constraints required for tiling compatibility make the solid volume fraction dependent

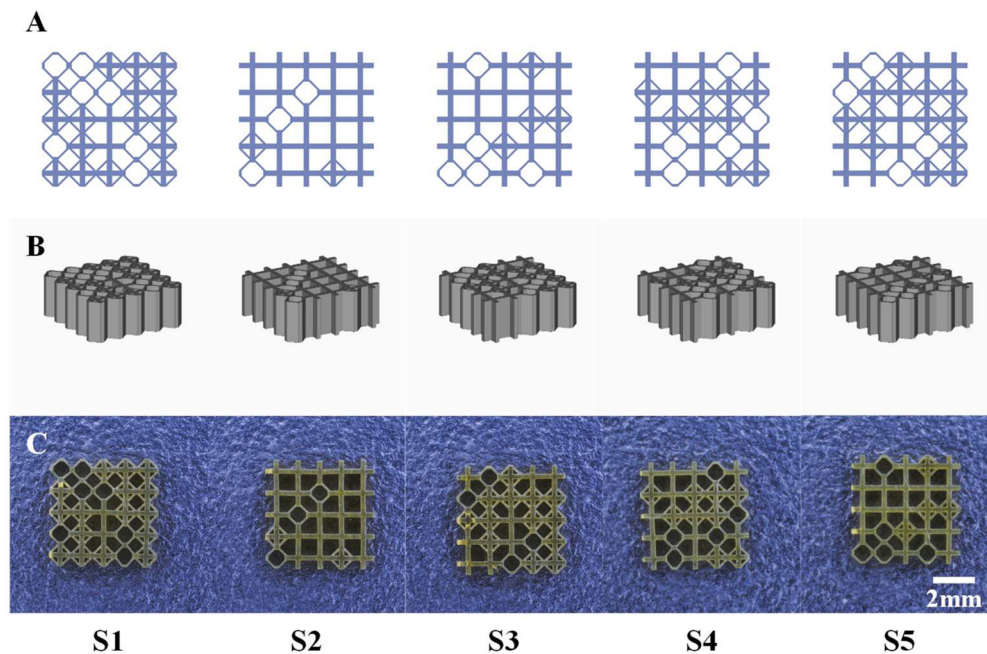


Figure 8. Representative samples (S1–S5). (A) Schematic of the designed structures (S1–S5); (B) Corresponding 3D models (S1–S5); (C) Photographs of the 3D printing samples (S1–S5).

on unit cell type. Therefore, structural configuration and relative density are coupled in the present parameter setting. The relative density is therefore calculated as: $\rho = \rho_{\text{tris}} \cdot f_{\text{tris}} + \rho_{\text{quads}} \cdot f_{\text{quads}} + \rho_{\text{oct}} \cdot f_{\text{oct}}$, where f_{tris} , f_{quads} and f_{oct} denote the fractions of tris, quads, and oct unit cells, respectively, and $\rho_{\text{tris}} = 0.5$, $\rho_{\text{quads}} = 0.36$, $\rho_{\text{oct}} = 0.22$; the relative densities of the five samples are listed in Table S2. Consequently, the load-bearing topology and connectivity were considered to be retained, allowing the differences in the elastic modulus among samples S1–S5 to be primarily attributed to the designed tiling topology rather than geometric deviations.

For all samples, a distinct near-linear elastic regime was observed at small strains; the in-plane elastic modulus was determined from the slope of the stress-strain response over the 1.0–2.5% strain interval. With further compression, the response transitioned to a nonlinear regime characterized by either a peak stress or a stress plateau, which is typical of cellular architectures and is governed by progressive local buckling, cell-wall/strut bending, and subsequent collapse and contact within the lattice (Figure 9).^{43,44}

As illustrated in Figure 10, a comparison is presented between the experimental modulus data of samples S1–S5 in the x and y directions and the data from the FEA database. A comparison of the FEA data with the

experimental data reveals that the smallest deviation occurs in the x direction of sample S1, where the difference between the FEA data and the experimental data (EXP) is only 0.9%. The most significant deviation is observed in the y direction for sample S2, where the discrepancy between the FEA and the EXP is 19.4%. These results indicate that the simulation-based evaluation of the elastic modulus (E_x and E_y), together with the subsequent data-driven screening, provides reliable guidance for selecting structures with targeted elastic modulus. In Figure S3 and Table S3, the elastic modulus (E_x and E_y) of the five samples obtained from UCAE-FCNN, UCFS-FCNN, FEA and experiments are further compared. The results show good overall agreement among the ML predictions, FEA results, and experimental tests.

The ML model was trained using a structure-property database. Consistency between the predicted or screened values and the experimental measurements therefore provided validation of the overall closed-loop workflow. Within this workflow, geometry generation and simulation were employed to construct the training database, and the trained model was subsequently applied for rapid prediction of elastic modulus (E_x and E_y) and inverse screening. Experimental verification further confirmed that the selected structures could be physically realized while achieving the targeted elastic modulus levels within

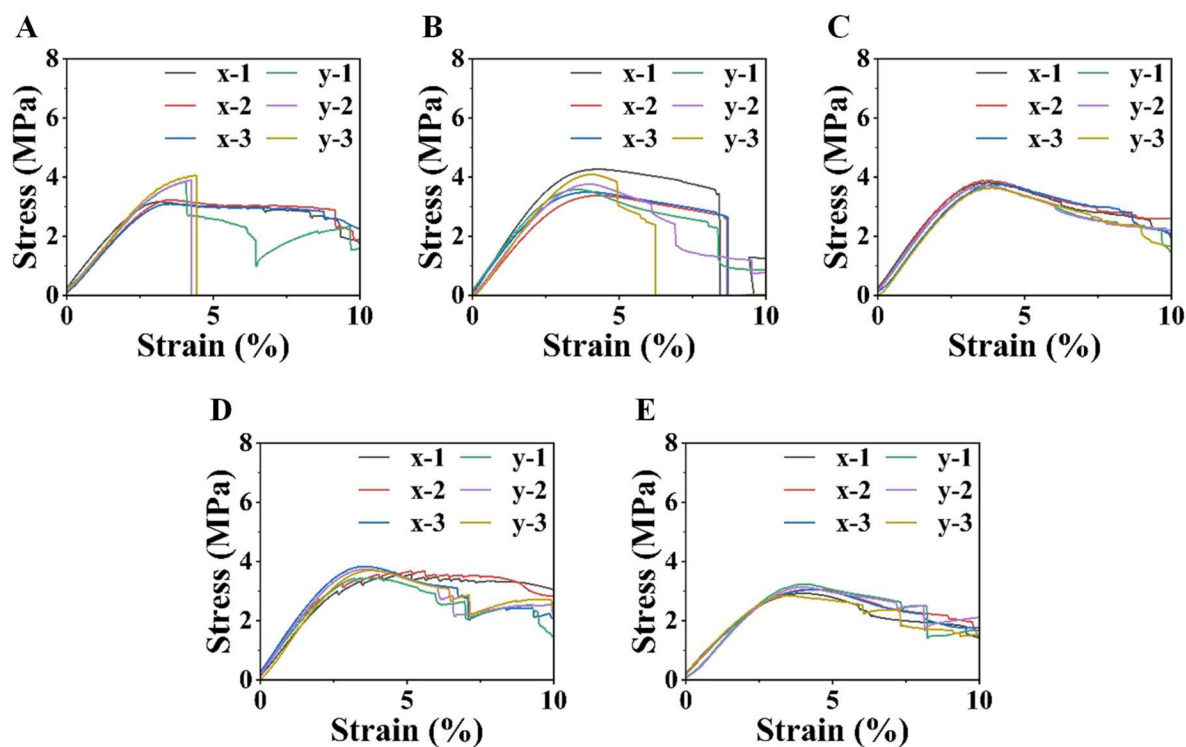


Figure 9. Representative compressive stress-strain curves of S1–S5 under loading along the x and y directions: (A) S1, (B) S2, (C) S3, (D) S4, (E) S5

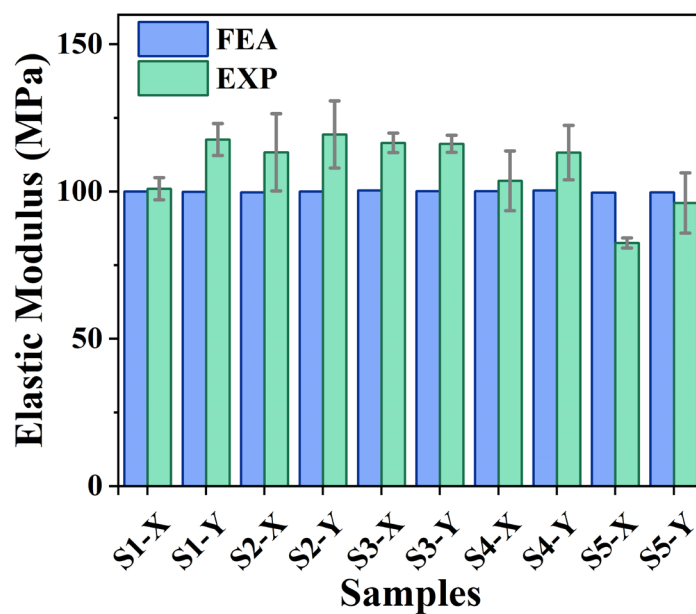


Figure 10. Comparison of modulus between compression tests and FEA
Abbreviations: EXP: Experimental data; FEA: Finite element analysis.

a mean relative deviation of 20%.

4. Conclusion

This paper presents a data-driven design framework for programmable ET structures to expand the structural design beyond conventional periodic bone implant lattices and to enable prediction and inverse screening of the elastic modulus (E_x and E_y) by ML. The main conclusions can be summarized as follows:

- (1) Programmable ET structures enable high geometric freedom with controllable in-plane elastic modulus. A total of 10,000 distinct structures generated from tris, quad, and oct unit cells demonstrated that E_x and E_y can be tuned through tiling configuration within a single material system.
- (2) UCAE model significantly improves the accuracy of directional structure-property prediction. Using the UCAE model, the FCNN achieved prediction accuracies of $R^2 \approx 0.99$ for both E_x and E_y , with MAEs of 1.37 MPa for E_x and 1.36 MPa for E_y , substantially outperforming the UCFS model.
- (3) Data-driven inverse screening reliably retrieves structures with targeted elastic modulus. Structures identified via a KNN strategy exhibited deviations within 20% between experimental measurements and numerical predictions, confirming the effectiveness of the proposed closed-loop framework.

Overall, the proposed framework establishes a scalable pathway for the forward prediction and inverse screening of architected bone implant lattices based on their in-plane elastic modulus (E_x and E_y). As a future direction, this 2D ET-based framework will be extended to fully 3D structures to evaluate directional elastic modulus under realistic 3D mechanical conditions. The approach will also be expanded from the current linear elastic modulus prediction and inverse screening to nonlinear mechanical properties, including z-axis modulus (E_z), strength, yield behavior, energy absorption, and porosity-related descriptors. In addition, further work will focus on clarifying the underlying mechanical mechanisms by which different tiling configurations regulate load transfer, deformation, and directional stiffness, thereby providing a stronger basis for future orthopedic scaffold and implant design.^{45–47}

Acknowledgments

The authors gratefully acknowledge Lingwen Hua and Zihao Zhao for their non-financial support, particularly

for their assistance with manuscript preparation and constructive discussions.

Funding

This work was supported by the National Natural Science Foundation of China (52273278) and the Natural Science Foundation of Liaoning Province (2024-MSBA-66).

Conflict of interest

Xing Zhang is an Editorial Board Member of this journal, but was not in any way involved in the editorial and peer-review process conducted for this paper, directly or indirectly. Separately, other authors declared that they have no known competing financial interests or personal relationships that could have influenced the work reported in this paper.

Author contributions

Conceptualization: Xing Zhang, Zongze Wu

Formal analysis: Zongze Wu, Lei Cao

Investigation: Zongze Wu, Xiaoxiao Dong

Methodology: Zongze Wu, Xing Zhang

Writing—original draft: Xiaoxiao Dong, Zongze Wu

Writing—review & editing: Xing Zhang, Deliang Zhang

Ethics approval and consent to participate

Not applicable.

Consent for publication

Not applicable.

Availability of data

The data presented in this study are available from the corresponding authors upon reasonable request.

References

1. Huiskes R, Weinans H, Rietbergen BY. The Relationship Between Stress Shielding and Bone Resorption Around Total Hip Stems and the Effects of Flexible Materials. *Clin Orthop Relat Res*. 1992;274.
doi: 10.1097/00003086-199201000-00014
2. Zadpoor AA. Mechanical performance of additively manufactured meta-biomaterials. *Acta Biomater*. 2019;85:41–59.
doi: 10.1016/j.actbio.2018.12.038
3. Evans FG. Mechanical Properties of Bone. Thomas; 1973. Available from https://www.google.co.jp/books/edition/_/EqATngEACAAJ?hl=zh-CN&sa=X&ved=2ahUKewj8x6ur u62TAxWLoa8BHsf4KOkQre8FegQICRAC [Last accessed on 2026 Mar 25].

4. Currey JD. Bones: Structure and Mechanics. Princeton University Press. 2002. Accessed January 11, 2026. Available from <https://www.jstor.org/stable/j.ctt4cg9wv> [Last accessed on 2026 Mar 25].
5. Rho JY, Kuhn-Spearing L, Zioupos P. Mechanical properties and the hierarchical structure of bone. *Med Eng Phys*. 1998;20(2):92-102.
doi: 10.1016/S1350-4533(98)00007-1
6. Ashman RB, Jee YR. Elastic modulus of trabecular bone material. *J Biomech*. 1988;21(3):177-181.
doi: 10.1016/0021-9290(88)90167-4
7. Rho JY, Ashman RB, Turner CH. Young's modulus of trabecular and cortical bone material: Ultrasonic and microtensile measurements. *J Biomech*. 1993;26(2):111-119.
doi: 10.1016/0021-9290(93)90042-D
8. Zysset PK, Edward Guo X, Edward Hoffler C, et al. Elastic modulus and hardness of cortical and trabecular bone lamellae measured by nanoindentation in the human femur. *J Biomech*. 1999;32(10):1005-1012.
doi: 10.1016/S0021-9290(99)00111-6
9. Arabnejad S, Johnston B, Tanzer M, et al. Fully porous 3D printed titanium femoral stem to reduce stress-shielding following total hip arthroplasty. *J Orthop Res*. 2017;35(8):1774-1783.
doi: 10.1002/jor.23445
10. Ibrahim P, Jameekornkul P, Panesar A, et al. The utility of additively manufactured β -Ti latticed hip implants in reducing femoral stress shielding: A finite element study. *J Mech Behav Biomed Mater*. 2025;168:106999.
doi: 10.1016/j.jmbbm.2025.106999
11. Qin Y, Jing Z, Zou D, et al. A metamaterial scaffold beyond modulus limits: enhanced osteogenesis and angiogenesis of critical bone defects. *Nat Commun*. 2025;16(1):2180.
doi: 10.1038/s41467-025-57609-9
12. Safavi S, Gray HA, Lee PVS. Design and optimisation of patient-specific porous femoral stems. *J Orthop Surg*. 2025;20(1):1002.
doi: 10.1186/s13018-025-06389-5
13. Kadkhodapour J, Montazerian H, Darabi ACh, et al. Failure mechanisms of additively manufactured porous biomaterials: Effects of porosity and type of unit cell. *J Mech Behav Biomed Mater*. 2015;50:180-191.
doi: 10.1016/j.jmbbm.2015.06.012
14. García-Gareta E, Coathup MJ, Blunn GW. Osteoinduction of bone grafting materials for bone repair and regeneration. *Bone*. 2015;81:112-121.
doi: 10.1016/j.bone.2015.07.007
15. Bose S, Vahabzadeh S, Bandyopadhyay A. Bone tissue engineering using 3D printing. *Mater Today*. 2013;16(12):496-504.
doi: 10.1016/j.mattod.2013.11.017
16. Benedetti M, du Plessis A, Ritchie RO, et al. Architected cellular materials: A review on their mechanical properties towards fatigue-tolerant design and fabrication. *Mater Sci Eng R Rep*. 2021;144:100606.
doi: 10.1016/j.mser.2021.100606
17. Maevskaia E, Guerrero J, Ghayor C, et al. Triply periodic minimal surface-based scaffolds for bone tissue engineering: A mechanical, in vitro and in vivo Study. *Tissue Eng Part A*. 2023;29(19-20):507-517.
doi: 10.1089/ten.tea.2023.0033
18. Ghazlan A, Ngo T, Le VT, et al. A bio-mimetic cellular structure for mitigating the effects of impulsive loadings-A numerical study. *J Sandw Struct Mater*. 2021;23(6):1929-1955.
doi: 10.1177/1099636220908581
19. Jia Y, Liu K, Zhang XS. Modulate stress distribution with bio-inspired irregular architected materials towards optimal tissue support. *Nat Commun*. 2024;15(1):4072.
doi: 10.1038/s41467-024-47831-2
20. Jia Y, Liu K, Zhang XS. Topology optimization of irregular multiscale structures with tunable responses using a virtual growth rule. *Comput Methods Appl Mech Eng*. 2024;425:116864.
doi: 10.1016/j.cma.2024.116864
21. Grünbaum B, Shephard GC. Tilings by Regular Polygons. *Math Mag*. 1977;50(5):227-247.
doi: 10.1080/0025570X.1977.11976655
22. De Las Peñas MLAN, Tomenes MD, Abila AKM. Creating planar k-isogonal tilings: 29th Asian Technology Conference in Mathematics, ATCM 2024. *Proc Asian Technol Conf Math*. 2024;52-66. Available from <https://research.ateneo.edu/en/publications/creating-planar-k-isogonal-tilings/> [Last accessed on 2026 Mar 25].
23. Max N. Constructing and visualizing uniform tilings. *Computers*. 2023;12(10):208.
doi: 10.3390/computers12100208
24. Roberts AP, Garboczi EJ. Elastic moduli of model random three-dimensional closed-cell cellular solids. *Acta Mater*. 2001;49(2):189-197.
doi: 10.1016/S1359-6454(00)00314-1
25. Li K, Gao XL, Subhash G. Effects of cell shape and cell wall thickness variations on the elastic properties of two-dimensional cellular solids. *Int J Solids Struct*. 2005;42(5):1777-1795.
doi: 10.1016/j.ijsolstr.2004.08.005

26. Li K, Gao XL, Wang J. Dynamic crushing behavior of honeycomb structures with irregular cell shapes and non-uniform cell wall thickness. *Int J Solids Struct.* 2007;44(14):5003-5026.
doi: 10.1016/j.ijsolstr.2006.12.017
27. Grünbaum B, Shephard GC. *Tilings and Patterns*. Courier Dover Publications. 1987. Available from https://archive.org/details/isbn_0716711931/page/n1/mode/1up [Last accessed on 2026 Mar 25].
28. Mahato V, Chatterjee S, Nyabadza A, *et al.* Layer porosity in powder-bed fusion prediction using regression machine learning models and time-series features. *Int J AI Mater Des.* 2024;1(3):33-49.
doi: 10.36922/ijamd.4812
29. Lew AJ, Jin K, Buehler MJ. Designing architected materials for mechanical compression via simulation, deep learning, and experimentation. *Npj Comput Mater.* 2023;9(1):80.
doi: 10.1038/s41524-023-01036-1
30. Ha CS, Yao D, Xu Z, *et al.* Rapid inverse design of metamaterials based on prescribed mechanical behavior through machine learning. *Nat Commun.* 2023;14(1):5765.
doi: 10.1038/s41467-023-40854-1
31. Zheng L, Karapiperis K, Kumar S, *et al.* Unifying the design space and optimizing linear and nonlinear truss metamaterials by generative modeling. *Nat Commun.* 2023;14(1):7563.
doi: 10.1038/s41467-023-42068-x
32. Yang Z, Yu CH, Buehler MJ. Deep learning model to predict complex stress and strain fields in hierarchical composites. *Sci Adv.* 2021;7(15):eabd7416.
doi: 10.1126/sciadv.abd7416
33. Jo J, Park M, Kang S, *et al.* Data-driven prediction of strain fields in auxetic structures and non-contact validation with mechanoluminescence for structural health monitoring. *Int J AI Mater Des.* 2024;1(2):48-60.
doi: 10.36922/ijamd.3539
34. Luan S, Chen E, John J, *et al.* A data-driven framework for structure-property correlation in ordered and disordered cellular metamaterials. *Sci Adv.* 2023;9(41):ead1453.
doi: 10.1126/sciadv.adi1453
35. Shaikeea AJD. Exploration of truss metamaterials with graph based generative modeling. *Nat Commun.* 2023;14(1):7565.
doi: 10.1038/s41467-023-43217-y
36. Meyer PP, Bonatti C, Tancogne-Dejean T, *et al.* Graph-based metamaterials: Deep learning of structure-property relations. *Mater Des.* 2022;223:111175.
doi: 10.1016/j.matdes.2022.111175
37. Jiawei Wang, Yanqin Liu, Limei Yan, *et al.* Fractional sub-equation neural networks (fSENNs) method for exact solutions of space-time fractional partial differential equations. *Chaos* 2025;35(4):043110.
doi: 10.1063/5.0259937
38. Xie XR, Zhang RF. Neural network-based symbolic calculation approach for solving the Korteweg-de Vries equation. *Chaos Solitons Fractals.* 2025;194:116232.
doi: 10.1016/j.chaos.2025.116232
39. Liu K, Sun R, Daraio C. Growth rules for irregular architected materials with programmable properties. *Science.* 2022;377(6609):975-981.
doi: 10.1126/science.abn1459
40. Gibson LJ, Ashby MF. *Cellular Solids: Structure and Properties*. 2nd ed. Cambridge University Press. 1997.
doi: 10.1017/CBO9781139878326
41. Bastek JH, Kochmann DM. Inverse design of nonlinear mechanical metamaterials via video denoising diffusion models. *Nat Mach Intell.* 2023;5(12):1466-1475.
doi: 10.1038/s42256-023-00762-x
42. Lumpe TS, Stankovic T. Exploring the property space of periodic cellular structures based on crystal networks. *Proc Natl Acad Sci USA.* 2021;118(7):e2003504118.
doi: 10.1073/pnas.2003504118
43. Lamas I, Feijoo I, Gómez S, *et al.* Influence of nodal spheres on the mechanical behaviour of auxetic materials manufactured with PA12. *Materials.* 2025;18(24):5688.
doi: 10.3390/ma18245688
44. Gibson LJ. Biomechanics of cellular solids. *J. Biomech.* 2005;38(3):377-399.
doi: 10.1016/j.jbiomech.2004.09.027
45. Meza LR, Zelhofer AJ, Clarke N, *et al.* Resilient 3D hierarchical architected metamaterials. *Proc Natl Acad Sci.* 2015;112(37):11502-11507.
doi: 10.1073/pnas.1509120112
46. Kolken HMA, de Jonge CP, van der Sloten T, *et al.* Additively manufactured space-filling meta-implants. *Acta Biomater.* 2021;125:345-357.
doi: 10.1016/j.actbio.2021.02.020
47. Zhao D, Yu K, Sun T, *et al.* Material-structure-function integrated additive manufacturing of degradable metallic bone implants for load-bearing applications. *Adv Funct Mater.* 2023;33(16):2213128.
doi: 10.1002/adfm.202213128